Chapter 3

Effect of amphiphilic polymers on phase separating binary mixtures

3.1 Introduction

Much research is devoted to understanding the kinetics of phase separation of multicomponent mixtures due to its varied scientific and technical importance. A homogeneous mixture becomes thermodynamically unstable when quenched below the critical temperature [3,11,21] and shifts to an equilibrium state via phase-separating into the domains of various components [3,11,21,86]. These domains coarsen with time as it is energetically favorable in reducing the interfacial cost caused by the repulsive interaction between the incompatible components of the mixture. Thus, interfacial tension is the main driving force for phase separation kinetics [21]. We may anticipate that influencing the interfacial tension can be essential in determining the intriguing nonequilibrium dynamic behavior of the phase separation. Therefore, introducing amphiphilic macromolecules (surface active polymers well-known for their surfactant or compatibilizing properties) in the fluid mixture that can rapidly adsorb at the interfaces separating the growing domain plays a vital role. A typical surfactant or compatibilizer macromolecule is an amphiphile that generally has two different block structures [87–89], each having particular affinity to either one of the immiscible components of binary (AB) fluid [90–94]. Thus, when introduced in the binary mixture, they diffuse to the interface where they interact with their corresponding more favorable phases of the fluid [95–98]. The usual function of these molecules is to reduce the interfacial tension between A and B domains, thus facilitating chain dispersion, bio emulsion for drug delivery, stabilizing morphology against severe melt processing conditions, and enhancing adhesion between two phases [71,98].

Their presence can change the overall kinetics of phase separation of AB mixture [99–102]. The typical surfactants for AB mixtures such as simple fluids, polymer melts, and polymer networks are BCPs, MSPs, etc., comprised of two incompatible polymer chains [71]. In this work, we report the results of our DPD simulation study on phase separation kinetics of simple fluids incorporating surfactants of various architecture, composition ratios, and chain rigidity. The phase segregation kinetics has been studied extensively for AB [103] and ternary (ABC) [104] mixtures using different simulation techniques [105–107], experimental [108–113], and analytical methods [3,11,21]. It is now well-established that evolving AB-mixture segregates into A-rich and B-rich domains with a characteristic length scale $R(t)$, where t is time after the quench. During the late stages of evolution, $R(t)$ follows a power-law behavior [21], defined as: $R(t) \sim t^{\phi}$ where ϕ is the growth exponent. The growth of domains is a scaling phenomenon, *i.e.*, the domain morphologies statistically remain the same with time; only their scales change [3,11,21]. The dynamical scaling is exhibited by the two-point equal-time correlation function, $C(r,t)$, in terms of scaling behaviour as [3,21]: $C(r,t) = g(r/R(t))$ where $g(x)$ is a scaling function independent of time, and r is the spatial separation between the two points. The domain coarsening of the phase-separating system depends on the transport mechanism that drives the segregation. For more in details see the Sec. 1.5.

Despite having a better grasp of phase segregation kinetics for binary fluids, our understanding of the kinetics of segregation in liquids in the presence of amphiphilic molecules is even more limited. The cause might be the mixture's many components interacting in a competitive way, which would make the issue more complicated. Many theoretical [90,95,96] and numerical [91–96,100] studies have reported the phase segregation kinetics of binary mixture and surfactants based on the phase-field models or time-dependent Ginzburg–Landau models [90–96]. Those studies were performed either by considering a scaler field (a local density difference) for AB mixture and discrete particles with spin vectors for surfactants (hybrid or semi-microscopic model) [90,91]. Some studies are done by modeling two scalar fields: the local density difference between A and B fluids and the local surfactant density [92,94–96]. In other cases two scalar fields are considered as in the previous case, and one a vector order parameter field provides the local average orientation of the surfactant molecules [93]. The primary outcomes were the (a) slowdown of the growth kinetics with surfactant density, (b) the dynamical scaling of the evolution morphologies [90–94]. Note that those analyses were performed in $d = 2$ systems and the purely diffusive growth regime.

Further, experimental studies [97,98] demonstrate the similar slowing down of biomolecules phase separation in the presence of amphiphilic proteins that coat the biomolecules resembling surfactant. However, their focus was to study the equilibrium properties of the system. In the hydrodynamic lattice–gas simulations of binary mixtures (oil-water) with surfactants in $d = 2$ [101] and $d = 3$ [102], Boghosian et al. observed a crossover from $\phi \simeq 1/3$ at early times to $\phi \simeq 2/3$ at late times for the low surfactant concentration, and slow logarithmic growth $(R(t \sim (\ln t)^{\phi})$ at moderate surfactant concentration was observed [101,102]. At higher surfactant concentrations, domain growth was arrested, and their data showed a good agreement with a stretched exponential fit. They have also illustrated that the late time length scale which is inversely proportional to surfactant density [102].

Note that the phase-field (coarse-grained) techniques discussed above use uncontrolled approximations to model the velocity field. On the other hand, the MD approach has the advantage of naturally incorporating flow fields and integrating true hydrodynamics in the system. Therefore, MD is frequently used to understand dynamics problems at the atomistic level. In an MD simulation work, the phase separation kinetics of a simple binary mixture in the presence of surfactants [99] was studied using the Nose-Hoover thermostat to preserve the system's hydrodynamics. The work is performed on a two-dimensional system, and the surfactants considered were diatomic molecules [99]. Their results exhibited a non-algebraic [99], slow domain growth without the diffusive growth exponent at early times; the length scale showed saturation with increasing surfactant concentration. However, regardless of the use of conventional MD simulation, it has a remarkably high computational cost to probe a higher length and time scale for an evolving system. For example, the viscous hydrodynamics regime has been reported recently in $d = 3$ *via* MD simulations [103,104,114,115]; though, the inertial hydrodynamics regime has still not been observed either by MD simulation in $d = 3$ or experiments.

In this regard, the DPD simulation technique [54–57] has a considerable advantage over MD simulation; it is well known to preserve the hydrodynamics with a few hundred particles only and is more often used to simulate a system over a higher length and time scale [56,57,106].

Though most of the works noted above for binary fluid and surfactant mixtures are investigated in $d = 2$, our knowledge of $d = 3$ systems is highly limited for many different and essential surfactant topologies. Therefore, this paper reports a comprehensive DPD simulation study of phase separation kinetics of simple AB fluid and amphiphilic polymer

(CD) mixtures in $d = 3$. We consider A and B incompatible components of SF in equal ratios, AP consists of symmetric incompatible C and D chain blocks which are compatible with SF components A and B, respectively. More details are provided in the methodology section below. Herein, our focuses on the evolution morphologies of SFs and AP segregation across the SF interfaces, as well as their effects on the corresponding dynamical behaviors, which are characterized by various standard tools. To emphasize the structural properties, we measure the density variation, RDFs, spatial correlation functions, structure factors of segregating SF and AP for various compositions, topologies, and chain lengths.

In this chapter, we have structured our studies as follows: In Sec. 3.2, we present the model, the computational methodology, and the relevant simulation details, providing the background for our work. Sec. 3.3 describes the parameters for characterizing morphologies. We discuss our simulation results in Sec. 3.4, followed by the conclusions in Sec. 3.5.

3.2 Methodology and parameters' details

This Chapter employs the DPD simulation method for the study. For a detailed explanation of this method, polymer modeling, and SRP interactions, please refer to Chapter 2. In this section, we present the essential parameters employed in the simulations.

We consider a cubic simulation box of size, $L = 64$. The total number density of beads is set to $\rho = 3$. Thus, the total number of beads in the simulation box is $N = 3 \times 64^3 = 786432$. The periodic boundary condition is applied in all three directions. We comprehensively study the mixtures of different APs (CD) and simple binary (AB) fluids. The amphiphilic polymer comprises two parts: C is hydrophilic, and D is hydrophobic. We choose three different architectures of amphiphilic CD: BCP, RCP, and MSP as depicted in Fig. 3.1.

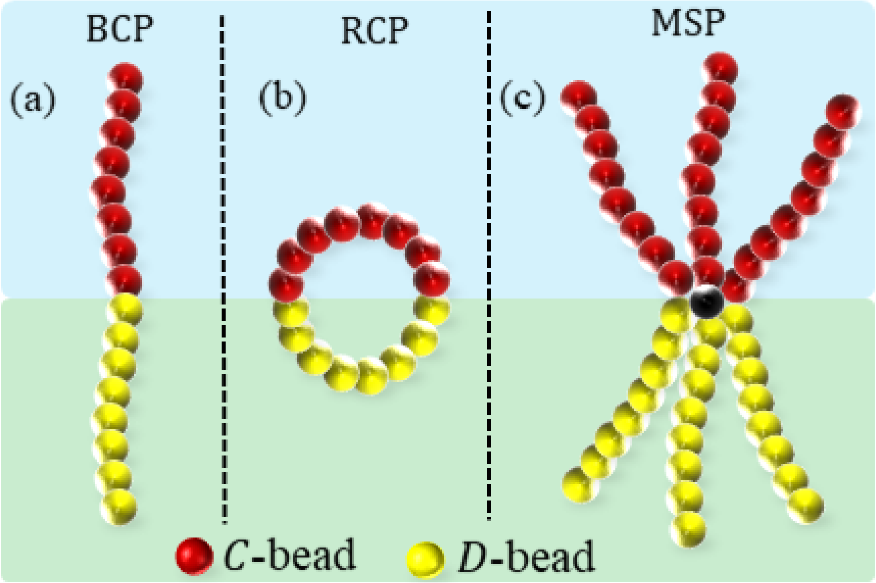

Fig. 3.1: A schematic illustration of the three distinct topologies with chain length $L_p = 16$ for amphiphiles: (a) BCP, (b) RCP, and (c) MSP configuration.

We consider three different chain lengths for each type of AP configuration (CD chain), $L_p = 8$, 16, and 32 and an MSP configuration having symmetric arrangement of C and D blocks. These three amphiphiles are different in terms of complexity due to their varying bond configurations and their structures. We perform a comparative study of binary (AB) fluid segregation kinetics in the presence of amphiphiles (CD). The following ratios, $N_A : N_B : N_{CD} = 1 : 1 : 1$ (critical composition), $2 : 2 : 1$, and $9 : 9 : 2$ (off-critical compositions), are considered for our study. Here, N_A, N_B, and N_{CD} represent the number of A-type, B-type, C- and D-type beads such that $N = N_A + N_B + N_{CD}$ and $N_{CD} = N_C + N_D$.

We set $a_{ij} = 25$ for any two beads of the same components. For immiscible binary SF components, $a_{AB} = 60$, and AP blocks, $a_{CD} = 60$. To model the compatibility (hydrophilicity) and incompatibility (hydrophobicity) of C and D beads with AB fluid, we assign $a_{AC} = 25$, $a_{BD} = 25$, and $a_{AD} = 45$, $a_{BC} = 45$, respectively. At time $t = 0$, the system is initially in a homogeneously mixed state, which is then quenched below the critical temperature. The system is then observed for $t = 2000\tau$ to understand its behavior in the far-from-equilibrium state.

3.3 Morphology characterizations

To characterize the morphologies of SF and surfactants across the interface of SF, we first calculate the RDF [116]: $g_{ij}(r) = \rho_{ij}(r)/\rho_j$, where g_{ij} represents the distribution of j beads around i beads with radial distance r. $\rho_{ij}(r)$ denotes the local density profile of j-type beads with spatial distance r, and ρ_j denotes the average total density of j-type beads. Secondly, we calculate the number density profile function [117] defined as $\rho_i(z) = n_z/V_z$ where $n_z = \sum_i \delta(z - \vec{r}_i \cdot \hat{z})$ is the number of i-type beads in a given slab of thickness $\Delta = 1.0$, and $V_z = L^2\Delta$ is the volume of the slab with L being the simulation box length in the $x-$ and $y-$ directions, respectively.

Further, to characterize the domain morphology, scaling properties and the length scale of SF, we compute the two-point equal-time correlation function $C(\vec{r}, t)$ [3,11,21,86]:

$$C(\vec{r}, t) = \langle \psi(\vec{r}_1, t)\psi(\vec{r}_2, t)\rangle - \langle \psi(\vec{r}_1, t)\rangle\langle \psi(\vec{r}_2, t)\rangle. \tag{3.1}$$

Here, $\psi(\vec{r}, t)$ is the order parameter for SF at time t and spatial position $\vec{r}$; $\langle \cdots \rangle$ denotes an ensemble average for five independent runs, and $\vec{k}$ is the scattering wave vector. As the system is isotropic, we consider spherically averaged versions of $C(\vec{r}, t)$ symbolized as $C(r, t)$ [3]. Similar to SF, we also conduct morphology characterization of surfactant (CD) fluid by computing the correlation function, $D(r, t)$ for order parameter, $\theta(\vec{r}, t)$ [3,106]

$$D(\vec{r}, t) = \langle \theta(\vec{r}_1, t)\theta(\vec{r}_2, t)\rangle - \langle \theta(\vec{r}_1, t)\rangle\langle \theta(\vec{r}_2, t)\rangle. \tag{3.2}$$

For calculating the order parameters, we map the continuum fluid configuration into nonoverlapping boxes of unit size and count the number of A, B, C, and D beads in each boxes as $n_A(\vec{r},t)$, $n_B(\vec{r},t)$, $n_C(\vec{r},t)$, and $n_D(\vec{r},t)$, respectively. The order parameters $\psi(\vec{r},t)$, and $\theta(\vec{r},t)$ are defined as:

$$\psi(\vec{r},t) = \frac{n_A(\vec{r},t) - n_B(\vec{r},t)}{n_A(\vec{r},t) + n_B(\vec{r},t)}. \tag{3.3}$$

We assign $\psi(\vec{r},t) = +1$ or -1 or 0 when a unit box is populated mainly by A or B or C and D-type beads. On the other hand, we set $\theta(\vec{r},t) = \psi(\vec{r},t)^2$ such that $\theta(\vec{r},t) = +1$ or 0 corresponding to either AB or CD phases, respectively. We assign each $\psi(r,t)$ value the same probability when a unit box has an equal number of A, B, and CD beads [103,106]. Since the nature of the system is isotropic, we use spherically averaged versions of $C(\vec{r},t)$ and $D(\vec{r},t)$ denoted as $C(r,t)$ and $D(r,t)$, respectively.

The primary imprint of a characteristic length scale, $R(t)$, on a phase-separating system leads to its dynamic scaling behavior [3,21]. Therefore, morphology characterization functions such as the correlation function is typically utilized to compute the length scale and the scaling functions [3,21,92,99]. The length scale calculation is defined as the distance at which the correlation function reduces to a certain fraction of its maximum value ($C(0,t) = 1$ and $D(0,t) = 1$) [3,21]. We compute the length scale from the first zero-crossing [3] of the correlation functions, $C(r,t)$, and 0.1 crossing for $D(r,t)$.

In simple binary fluid mixtures, domain growth is a rapid process driven by interfaces [106]. The growth kinetics follow the crossover from diffusive → viscous hydrodynamic → inertial hydrodynamic growth regimes; the diffusive growth regime, however, is very short-lived in DPD simulations [106]. In this chapter, we are interested in observing how the phase-separation dynamics of binary fluids change with the introduction of amphiphiles that quickly settle at the interface of fluid mixture components. To comprehensively understand the problem, we have sub-categorized it into three sub-sections, tackling different questions in each section below.

3.4 Numerical results and discussion

3.4.1 Effect of different topologies of amphiphilic polymers

We consider the case where $L_p = 16$ for BCP and RCP (8 beads of each C-type and D-type beads). In the case of MSP, we have six polymer chains of equal length covalently connected with one central bead with alternating arms consist of either C or D beads. Thus, the total number of beads for one MSP molecule is 49; however, in the analogy with BCP and RCP molecule's chain length, we may consider MSP molecule is made of three BCP chains with $L_p = 16$, as depicted in Fig. 3.1. The central bead is considered to be compatible with all the components. The MSP is anticipated to exhibit similar behavior to BCPs due to the formation of a BCP-like configuration. Herein, we fix the chain rigidity and stiffness of k_b=128, k_a=10 and a critical composition ratio $N_A : N_B : N_{CD} = 1 : 1 : 1$.

The first and second columns in Fig. 3.2 illustrate the evolution snapshots at early ($t = 500$) and late times ($t = 2000$) in the presence of APs of the type BCP, RCP, and MSP, respectively; the C and D blocks of AP are denoted in the red and yellow colors. Based on their compatibility, APs segregate across the interface of separating A and B phases, denoted in blue and green colors. It is evident from the snapshots that different sizes of A-B domains are obtained in the presence of different APs topologies. The SF domains seem slightly bigger in the case of MSP, followed by BCP and RCP. Though, they look less interconnected and bicontinuous in the case of MSP than in the other two cases. These differences are mainly due to the different structural constraints of APs. In the case of BCP, each block of type C and D have free ends. An RCP has a comparatively complicated structure, where the free ends are joined with a covalent bond, and there are no free ends. In the MSP molecule, all the arms are free at one end (same as in BCP), and the other ends are connected to a central bead (see Fig. 3.1(c)). It is significant to

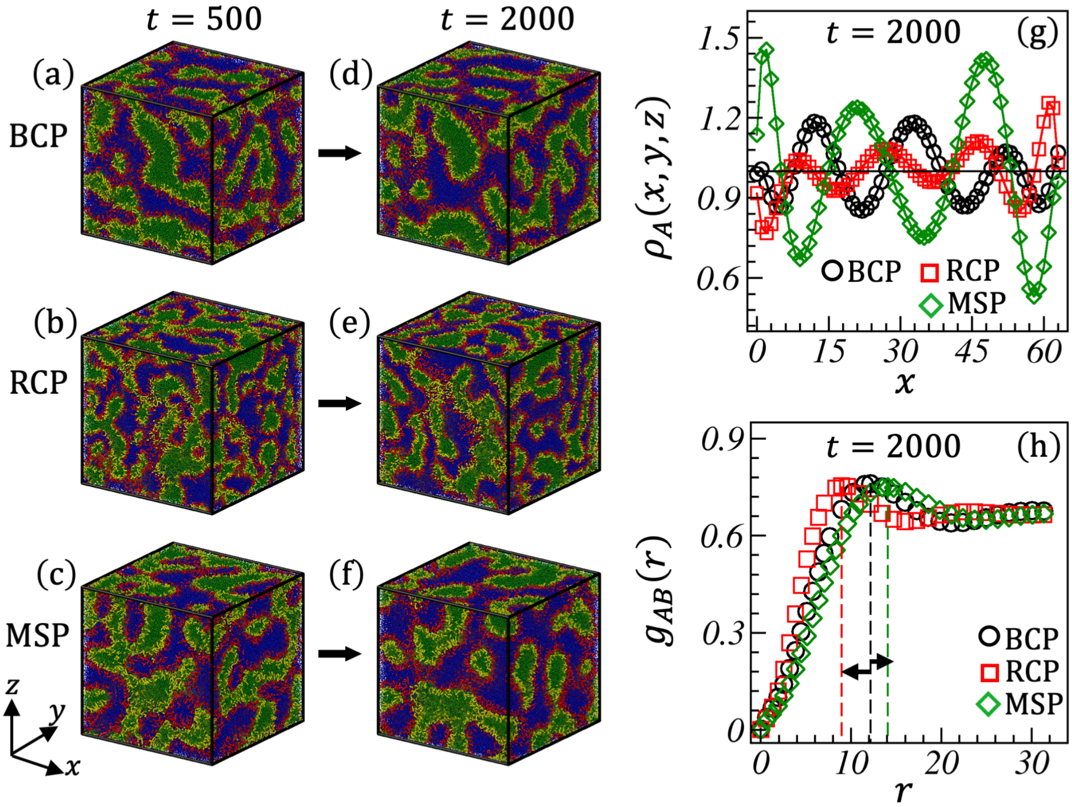

Fig. 3.2: Phase evolution morphology of simple binary (AB) fluid (the blue and green colors represent A and B-type beads) in the presence of APs (CD) of chain length $L_p = 16$ and with a critical ratio $N_A : N_B : N_{CD} = 1 : 1 : 1$. The red and yellow colors represent C and D-type beads. From the left, the first and the second columns represent the evolution snapshots at $t = 500$ and $t = 2000$, respectively. (g) The number density profile, $\rho_A(x, y, z)$, of A-type beads along the x-direction at a fixed yz, corresponding to the snapshots at $t = 2000$. (h) RDF, $g_{AB}(r)$, for B-type beads around A-type beads at $t = 2000$. See the text for full details

notice that at $t = 500$, a pure binary (AB) SF completely phase-separates into A and B domains, forming a single interface at the length and time scale of the simulation. This indicates that the inclusion of APs significantly slows down the evolution kinetics of SF. To illustrate this effect, we compare the morphologies at a later time, $t = 2000$, where the presence of APs generally results in smaller domain sizes. The average local density profile of A-type beads, $\rho_A(x, y, z)$, along the x-axis at a fixed yz-value is illustrated in Fig. 3.2(g) for late time $t = 2000$. In the presence of MSP, the amplitude of $\rho_A(x, y, z)$ is highest (green curve), indicating more enriched clusters of A-rich and B-rich phases. In contrast, BCP (black curve) shows a lower density profile, followed by RCP (red symbols), which has the lowest amplitude. To observe the spatial distribution of morphology, we plot the RDF, $g_{AB}(r)$, of B-type beads around A-type beads at $t = 2000$ as shown in Fig. 3.2(h). Notice that the RDFs do not overlap, highlighting the impact of different AP architectures on the phase-separated morphology of the SF. The RDF peak for RCP (red curve) is located at a smaller radial distance and is followed by BCP (black curve) and MSP (green curve). The primary peak of MSP (green curve) is located at a bigger r, indicating a larger domain size.

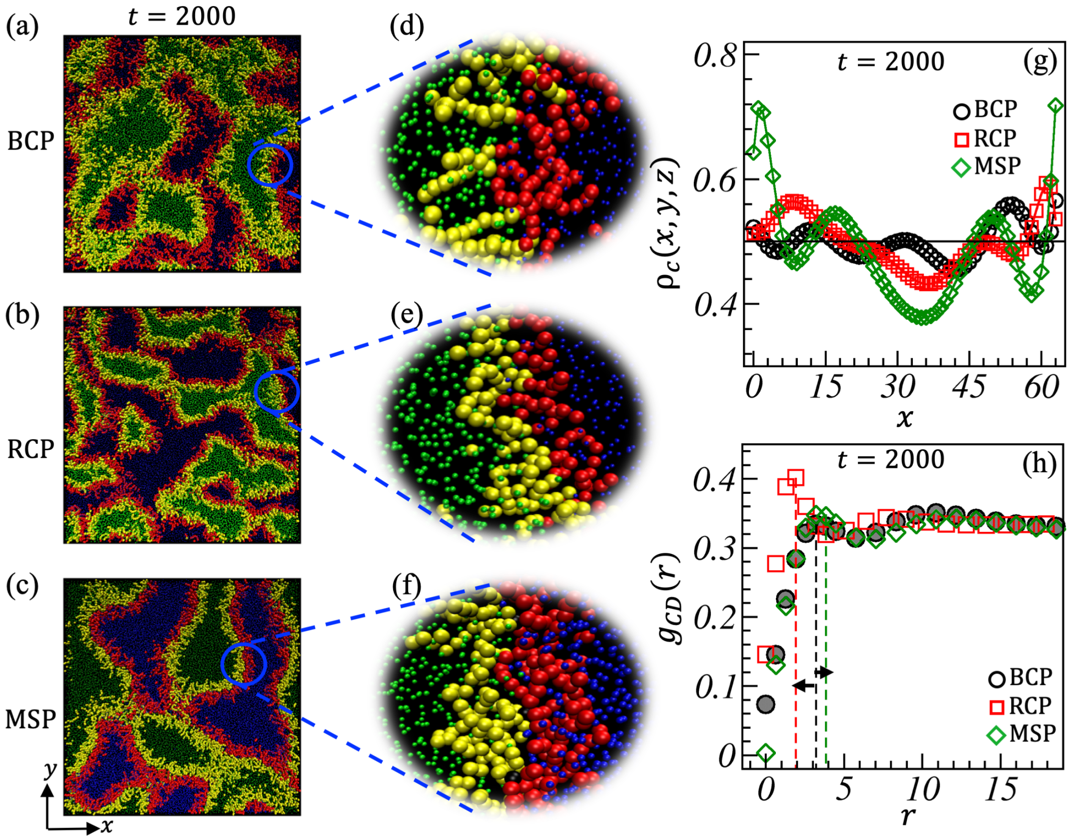

Fig. 3.3: Plots (a)-(c) shows the xy cross-section of the SF morphology as depicted in Figs. 3.2(d)–3.2(f). Plots (d)-(f) provides as enlarged view of specific region corresponding to the morphology in the first column. Plot (g) presents the variations in the number density of C-beads, $\rho_C(x, y, z)$ along the x-direction at $t = 2000$. Plot (h) illustrates the RDF, $g_{CD}(r)$, for D-beads surrounding C-beads at $t = 2000$.

The first column in Fig. 3.3 depicts the evolution snapshot along the xy-plane at a fixed $z = 32$ for the evolution snapshot shown in Fig. 3.2 at $t = 2000$. The second column provides an enlarged view of a specific region with enhanced clarity, highlighting the structure of APs and their distribution along the SF interface.

To characterize snapshots Figs. 3.2(d-f), we plot the variation in the number density profile of C-beads, $\rho_C(x, y, z)$, along the x-direction at a fixed yz value in Fig. 3.3(g). Notice that a larger domain size of the A or B phases can lead to a more significant accumulation of C or D-beads at their respective interfaces due to their favorable compatibility. Since a single MSP molecule corresponds to three BCP molecules, as shown in Fig. 3.1, it is evident that the amplitude of the local density profile of C-beads is higher for MSP compared to BCP. Conversely, a lower amplitude of the density profile, $\rho_C(x, y, z)$, in the presence of RCP indicates the existence of smaller domains, as shown in Fig. 3.2(e).

In Fig. 3.3(h), we explicitly display the RDF, g_{CD} of D-beads around C-beads across the SF interfaces. We notice that RDF peaks do not overlap due to the distinct spacial distribution of structurally different APs. The much lower g_{CD} peaks than g_{AB} indicate the loose clustering of APs across the interface. The main RDF peak for RCP appears at a lower r with higher peak strength than BCP and MSP. The reason could be that RCP flexibility is significantly subdued due to its topology that compelled RCP polymers to remain very close to A-B interfaces than other polymer molecules having free ends. This exact nature of RCP molecules can significantly restrict the transport of A and B beads across the interface, thus, leading to the formation of smaller A and B domains. The RDF for BCP and MSP chains are nearly similar, with a moderately higher first peak strength for the latter case as it has multiple C and D chain blocks connected to a single bead.

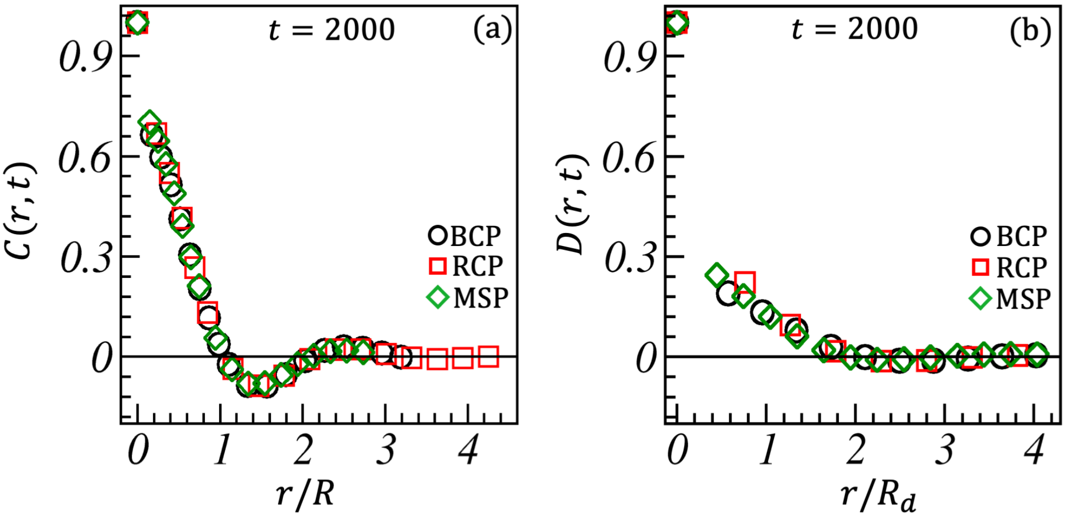

Fig. 3.4: Plot (a) shows the scaling plots of the correlation functions, $C(r,t)$ vs. $r/R(t)$ for the evolution shown in the second column of Figs. 3.2(d-f). (b) Shows the scaling plot of squared correlation function $D(r,t)$ vs. $r/R_d(t)$.

To get a better perspective of the evolution morphologies of SFs, we demonstrate the scaling functions, $C(r,t)$ vs. $r/R(t)$ on a linear scale in Fig. 3.4(a). The length scale, $R(t)$, is measured at the correlation function's first zero-crossing (indicated by a horizontal solid black line). All the curves are presented at a late time $t = 2000$. The excellent collapse of $C(r,t)$ data demonstrate statistically self-similar SF morphologies, even in the presence of APs of various architectures. Thus, as the dynamical scaling behavior of phase-separating SF is concerned, the effect of introducing various APs in the mixture is negligible. In a pure AB mixture ($N_{CD} = 0$), the correlation function decays linearly: $C(r,t) \simeq 1 - ar^{\eta} \cdots$ for $r \to 0$, due to scattering off sharp interfaces which is known as Porod's law [3,21,52,53]; here a is a constant factor and the surface exponent $\eta = 1$. However, we mark a distinct cusp behavior of $C(r,t)$ for $r \to 0$ for $N_{CD} \neq 0$ which shows that a non-Porod behavior. This is usually the consequence of APs scattering off rough or fuzzy domain interfaces.

In order to quantify the characteristics of the APs morphologies separated across the SF interface corresponding morphologies seen in Figs. 3.2(d-f), we plot the scaling function, $D(r, t)$ as a function of $r/R_d(t)$ on a linear scale in Fig. 3.4(b). A fast decrease of $D(r, t)$ suggests loose segregation of the C and D phases of APs. The more closely overlapping black and green curves in BCP and MSP's scaled $D(r, t)$ demonstrate statistically self-similar segregation. The $D(r, t)$ of RCP (red curve) varies marginally at smaller scaled lengths $r/R_d(t)$, indicating a minor variation in its segregation behavior relative to BCP and MSP. As a result, the topology of AP has a moderate effect on the scaling function $D(r, t)$.

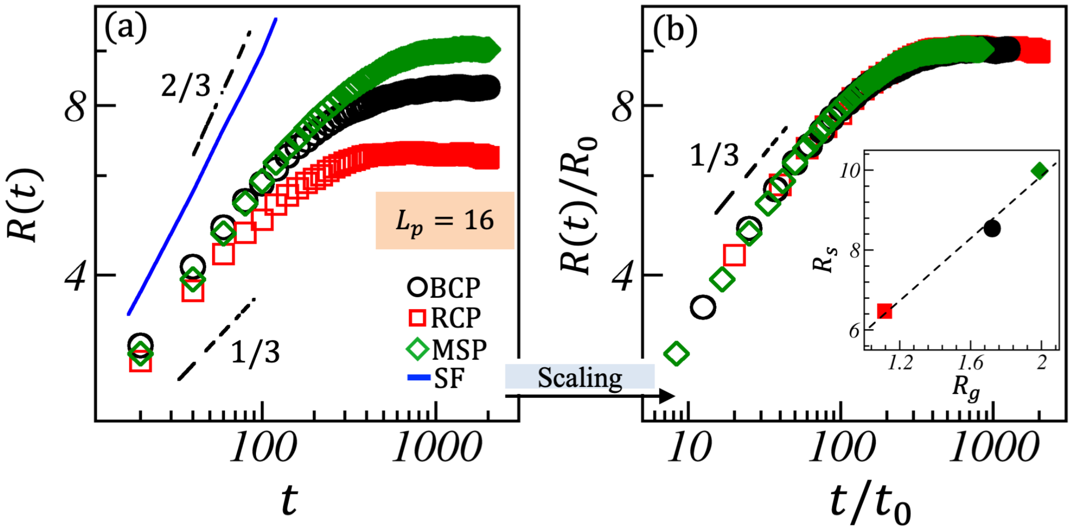

Fig. 3.5: The average domain size over time $R(t)$ corresponds to the evoution depicted in Figs. 3.2(d-f). The length scale, $R(t)$, and time, t, are scaled by a factor of R_0 and t_0 for each topology. The inset illustrates the corresponding saturation length, R_s, with varying effective sizes, R_g, of each topology.

Next, we investigate the results for the time dependence of average domain size. In Fig. 3.5(a), we plot $R(t)$ vs. t for SF morphology on a logarithmic scale. In our DPD simulation for a pure AB mixture ($N_{CD} = 0$, indicated by the blue solid line), the usual diffusive growth regime is very short-lived, and we can quickly access the viscous and inertial growth regimes at late times [59,106]. The presence of amphiphilic polymers drastically slows down the domain growth of SFs. The influence of distinct AP topologies on the transport of the AB fluid across the interface is evident from these plots.

In the presence of RCPs (red curve), the length scale behavior initially shows diffusive growth ($\phi \sim 1/3$) and then transitions to a frozen morphology, marked by a saturation length scale of about $R_s \sim 1.1$. A black dashed line with a slope of 1/3 is shown for reference. The length scales are marginally higher than diffusive growth in BCP (black curve) and MSP (green curve) presence at early times before the saturation at higher length scale is seen in Fig. 3.5(a).

When domain coarsening occurs in a d-dimensional system with a typical domain size $R(t)$, we can infer that the system volume, $V \sim N_d R^d$. Here, R^d represents the volume of an individual domain, and N_d denotes the total number of domains. Consequently, the area of the domain boundaries (the interface region) can be estimated as $A_d \sim N_d R^{(d-1)} \sim V/R$. Assuming domain coarsening arrests when there are ρ_p amphiphilic polymers per unit area of the interface, the saturation length can be approximated as follows,

$$R_s \sim \frac{\rho_p V}{N_p}, \tag{3.4}$$

where, the total number of amphiphilic polymeric chain is $N_p = N_{CD}/L_p$. This leads to the claim that there is a linear relationship between R_s and the size of AP's

$$R_s \sim \left(\frac{\rho_p V}{N_{CD}}\right) L_p, \tag{3.5}$$

where, the AP density remains constant, an inverse proportionality exists between the concentration of APs and Rs,

$$R_s \sim (\rho_p V L_p) \frac{1}{N_{CD}}, \tag{3.6}$$

while keeping the size of APs unchanged.

We extract the saturation length (R_s) for each curve from the saturation regimes in Fig. 3.5(a), assigning the values R_{s1}, R_{s2}, and R_{s3} to the black, red, and green curves, respectively. Our aim is to investigate the universality of the characteristic length across different AP topologies. We plot the scaling of domain length against t/t_0 in Fig. 3.5(b), where t_0 is the time scaling factor associated with the AP topologies. We compute the scaling factor for length so that all curves converge on the green curve: $R_0 = R_{s1}/R_{s3}$ for the black curve, $R_0 = R_{s2}/R_{s3}$ for the red curve, and $R_0 = R_{s3}/R_{s3}$ for the green curve. As a result, the black and red curves align with the green curve, indicating that the same universality class can describe the phase separation of simple fluids in the presence of BCP, RCP, and MSP along their interfaces. The inset of Fig. 3.5(b) shows the linear variation of R_s with the radius of gyration R_g [see Eq. 3.5] associated with different APs. Here, we compute R_g using the formula provided below:

$$R_g^2 = \frac{1}{N_{CD}} \sum_i (r_i - r_{cm})^2, \tag{3.7}$$

where, r_{cm} is the centre of mass of a polymeric chain.

Moreover, we analyze the effect of chain rigidity and stiffness of APs with different topologies on the phase separation kinetics of SF, while keeping the chain length constant at $L_p = 16$ and the critical composition $1:1:1$. We vary the bond rigidity and stiffness coefficients as follows: $(\kappa_a, \kappa_b) = (10, 128), (20, 256)$, and $(80, 1024)$. For this, we plot scaled correlation functions and average domain length for distinct values of (κ_a, κ_b) corresponding each type of APs in Fig. 3.6.

Obviously, increasing the rigidity of the polymeric chain within a finite range (from flexible to semi-flexible) can decrease its degree of freedom. This reduction can hinder the diffusion of APs to the interface, causing the process of APs settling at the interface to complete over time gradually. As a result, a pinning effect on SF phases occurs. During the same time frame, the inherently quicker segregation of SF leads to a larger domain size. Thus, increased AP stiffness facilitates the transport of SF components across the interface, thereby promoting the growth of larger length scales at higher rigidity.

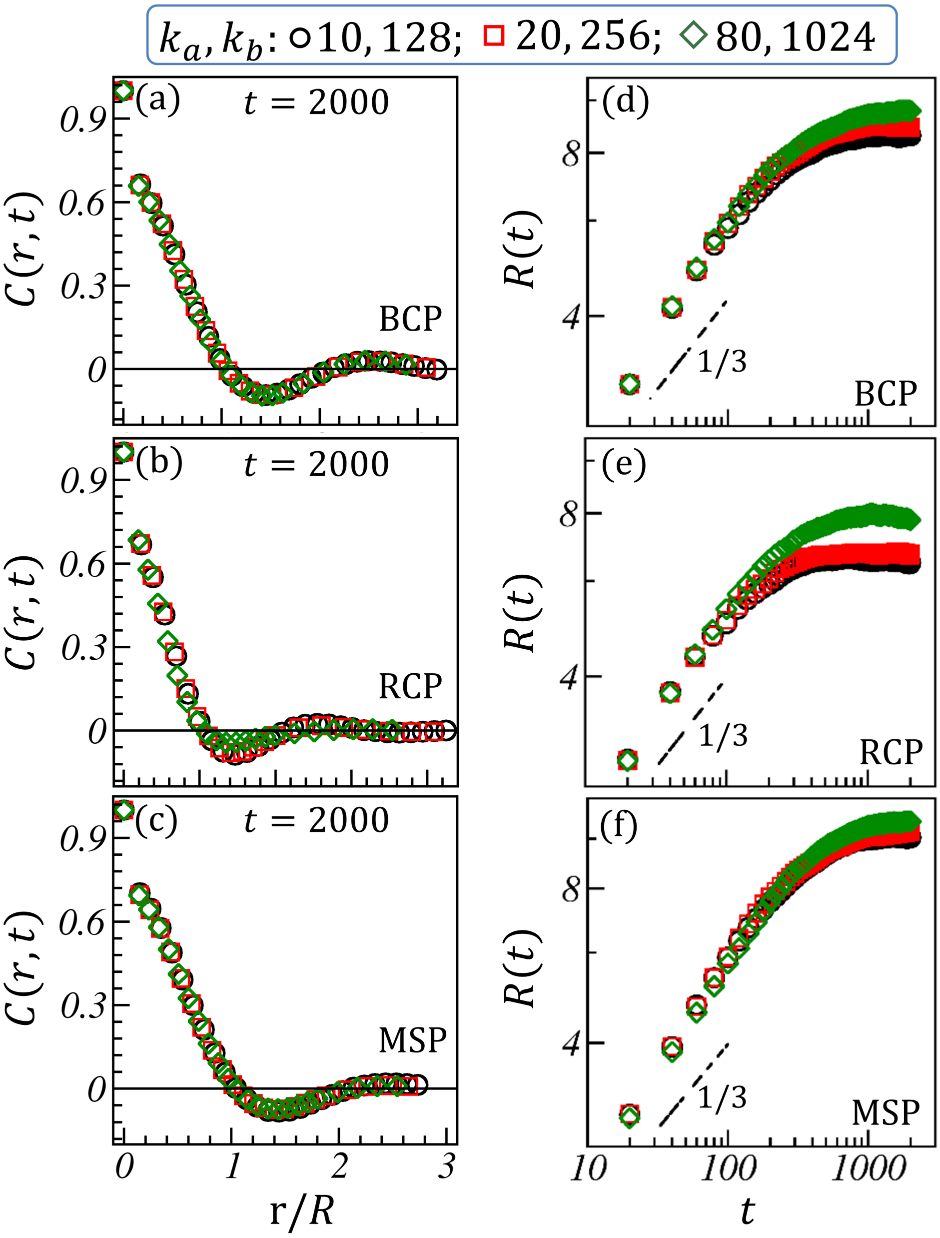

Fig. 3.6: The influence of chain rigidity and stiffness of APs on the domain coarsening of SF is demonstrated through the scaled correlation function, $C(r,t)$ vs. r/R. The solid black line indicates the zero-crossing point. The length scale $R(t)$ versus t for three distinct topologies: BCP, RCP, and MSP, where the black, red, and green symbols denote increasing chain rigidity: $(\kappa_a, \kappa_b) = (10, 128), (20, 256)$, and $(80, 1024)$.

Considering the configuration of BCP and MSP chain topologies, their respective morphologies at the interface are nearly identical for a constant stiffness. Thus, adjusting rigidity produces comparable alterations in SF's saturation length R_s obtained at later times. In Fig. 3.6(a) and Fig. 3.6(c), an excellent data overlap of the scaling functions $C(r,t)$ vs r/R at different rigidities depicts statistically self-similar SF morphology in the case of BCP and MSP, respectively. The associated length scale, represented by the green curve in Fig. 3.6(e), shows a more noticeable change in saturation. Moreover, it is noted that $R(t)$ tends to decrease non-monotonically at later times. The reason could lie in the notably fuzzy domain interface. The average domain sizes in the presence of RCPs are smaller compared to the other two cases with fixed rigidity. Consequently, as time progresses, the wetting of the interface with rigid RCPs becomes more prominent, potentially leading to a highly rough AB domain interface. Furthermore, the length scale curves depicted in Figs. 3.6(d-f) distinctly demonstrate the diffusive growth regimes (where $\phi \sim 1/3$) at early times for all cases of APs with varying rigidities (a reference line with a 1/3 slope indicating by the black dashed line).

3.4.2 Effect of amphiphilic polymer chain length

In this section, our objective is to study and investigate the influence of different chain lengths on the segregation kinetics of SF. We select three distinct AP chain lengths, denoted by $L_p = 8, 16$, and 32. Considering the critical composition $N_A : N_B : N_{CD} = 1:1:1$ with symmetric AP chains and fixed rigidity, $\kappa_a = 10$ and $\kappa_b = 128$. We have considered three different types of APs; however, our observations indicate that the effects of BCP and MSP show no significant differences regarding the segregation dynamics of SF. Consequently, this section focuses on and analyzes two cases involving BCP and RCP molecules.

We first analyze the effect of BCP chain length on the phase separation kinetics. The RDF of SF ($g_{AB}(r)$ vs. r) in Fig. 3.7(a) depicts the shifting of peak positions to higher values of r with the increase of BCP chain length, L_p. The shorter AP chains have the ability to diffuse to the AB interface more quickly due to the diffusion coefficient of

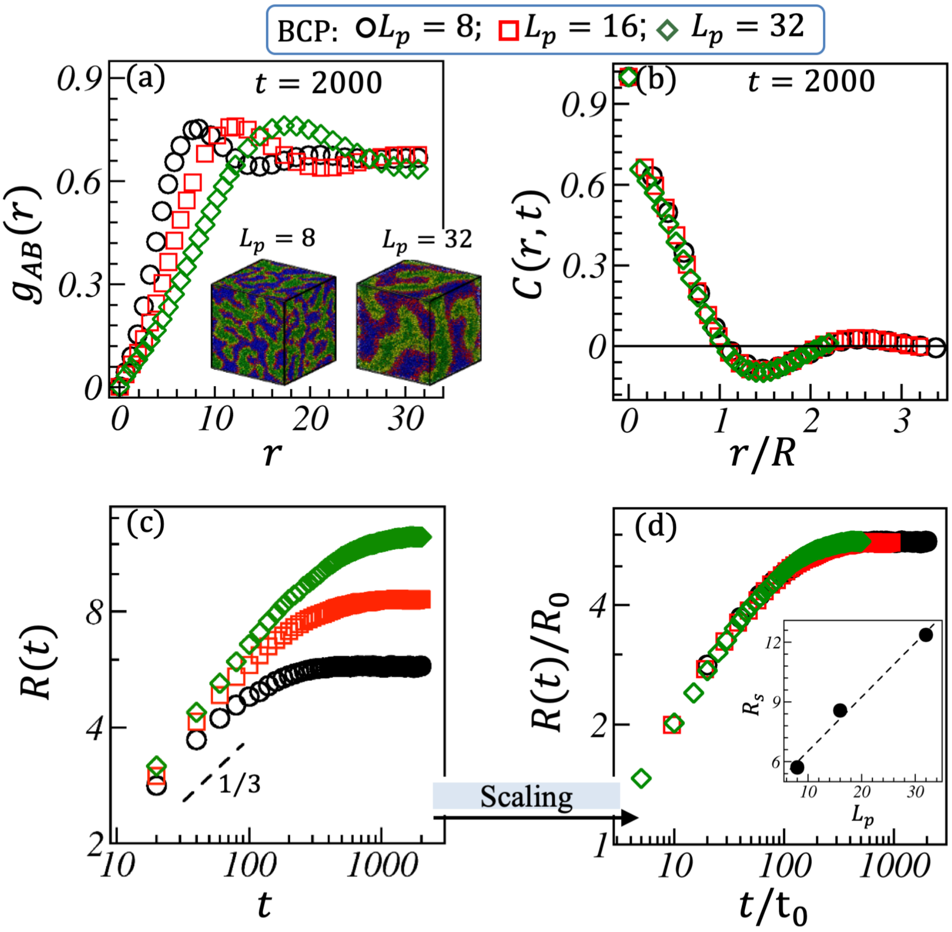

Fig. 3.7: The effect of various chain length ($L_p = 8, 16$, and 32) of BCP on SF phase separation kinetics is shown here. (a) Plot of $g_{AB}(r)$ versus r for different chain lengths. Snapshots illustrating the evolution corresponding to $L_p = 8$ and 32 are provided for visual reference. (b) Scaled correlation function $C(r,t)$ as a function of r/R at $t = 2000$. (c) Temporal variation of $R(t)$ for the three L_p values. The dashed black line shows a reference line with a 1/3 slope indicating diffusive growth. (d) Scaling of the length scale by the scale factor R_0 and time factor t_0 for each L_p curve. The inset illustrates a linear relationship between R_s and L_p.

polymers following $D \sim L_p^{-\nu}$, where $\nu = 1/2$ for melts and $\nu = 2/3$ for diluted solutions [118,119]. Note that the composition ratios are fixed; shorter chain length means more chains in the system and vice-versa. This can enable better coverage of the A-B interface by APs, thereby reducing the transport of A and B components across the interface and resulting in a smaller average domain size. Moreover, when shorter AP chains wet the interface, the interfacial tension decreases [83]. As a result, the transport of components

A and B across the interface is reduced, leading to a smaller average domain size, as shown in the snapshots provided in Fig. 3.7(a) for $L_p = 8$, compared to the larger average domain size for $L_p = 32$. Consequently, the peak position of $g_{AB}(r)$ at smaller r decreases with shorter chain lengths.

The scaled correlation function shown in Fig. 3.7(b) at a late time $t = 2000$ exhibits a significant superimposition of data from different curves. This indicates a coherent manifestation of dynamic scaling for BCPs with lengths $L_p = 8, 16$, and 32, as represented by the black, red, and green symbols. For higher chain length $(L_p = 32), C(r, t)$ displays reduced oscillatory behavior, diminishing at a much smaller r/R value compared to the other two cases. This observation implies a decrease in the number of interfaces within the system, suggesting the formation of larger SF domains. On the contrary, reducing chain length enhances the oscillatory characteristics in $C(r, t)$. These insights highlight BCP chain lengths' significant role in influencing SF's domain growth kinetics.

Figure 3.7(c) presents the time dependence domain length $R(t)$ for three distinct BCP chain lengths. The black dashed line corresponds to the diffusive growth regime ($\phi \sim 1/3$) at the initial growth period referred as a reference. The length scale follows the diffusive growth regime for shorter BCP chain lengths $L_p = 8$. However, the introduction of larger BCP chain lengths exhibits a slight deviation towards accelerated growth, as displayed by the red ($L_p = 16$) and green ($L_p = 32$) symbols. Gradually, $R(t)$ crosses over to a frozen length scale for all L_p. However, the crossover begins earlier for $L_p = 8$ and saturates at a much smaller fixed domain size than for larger BCP chains length. As explained earlier, this can be attributed to the rapid and enhanced interface coverage facilitated by a greater number of shorter BCPs. Conversely, the reduced diffusion coefficient for longer BCP chains leads to decreased interface coverage, resulting in the faster growth of SF phases. Despite the substantial differences in saturation length, it is noteworthy that the length scales follow the diffusive growth $\phi \sim 1/3$ before saturating.

Moreover, Fig. 3.7(d) suggests the plot of scaled average domain size, $R(t)/R_0$, against t/t_0. Herein, we observe $R_s \approx 5.7, 8.4$, and 12.4 correspond to the saturated domain sizes, and $t_0 \approx 1.0, 2.1$, and 4.0 represent the time scaling factors for three BCP chain lengths. The scaling plot displays excellent data superimpose, signifying that although the SF domain growth rate varies with distinct BCP chain lengths, show the statistical self-similarity. As a result, our observation suggests that the essential characteristics of the SF morphology remain unaffected by the presence of a specific BCP chain length. The inset displays the linear dependence of the saturation length R_s over L_p, as predicted by the theoretical aspect in Eq. 3.5.

In Fig. 3.8, we present the consequences of the presence of RCP of different sizes, $L_p = 8$, 16, and 32 denoted by the black, red, and green symbols, on the phase separation dynamics of AB and CD fluid components. Again, we choose the symmetric composition ratio, $N_A : N_B : N_{CD} = 1 : 1 : 1$ for the comparison at $t = 2000$. The RDF peaks depicted in Fig. 3.8(a) shift towards the higher values of r with the increment in chain lengths. For $L_p = 8$ shows smaller peak strength implying more dispersed A and B clusters. We show two evolution snapshots for $L_p = 8$ and 32 to illustrate the variations in cluster distribution and to give a more accurate visualization. The evolution for $L_p = 8$ shows a more diffuse arrangement of A and B clusters, in contrast to the denser distribution observed for $L_p = 32$.

The scaled correlation function, $C(r,t)$ vs. $r/R(t)$ in Fig. 3.8(b), shows a slight deviation from scaling for shorter chain length (black curve) compared to scaling $C(r,t)$ data at two higher RCP chain lengths. We observe that the dynamics are influenced by the presence of shorter RCP chain lengths. However, larger RCP chain length (red and green curves) shows excellent data overlap, indicating that they follow the same universality class. The black solid line displays first zero crossing of $C(r,t)$.

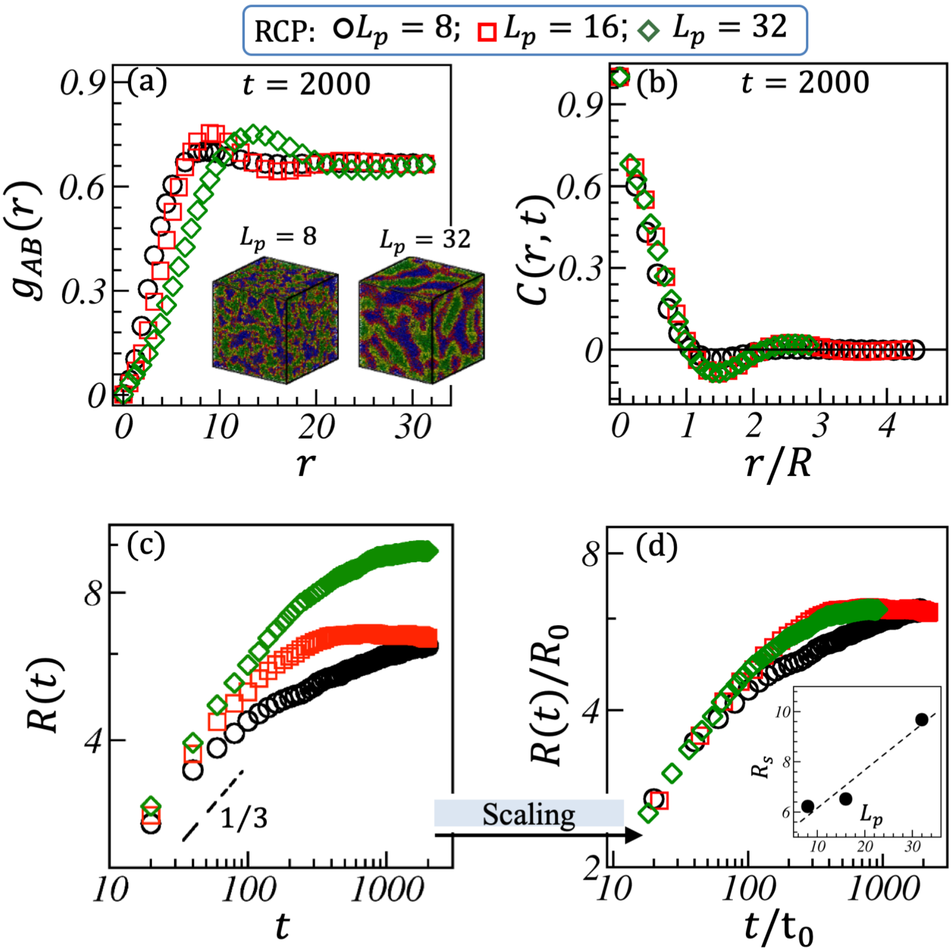

Fig. 3.8: Illustrating the influence of different RCP chain lengths: $L_P = 8$, 16, and 32 (indicated by various symbols) on phase separation kinetics at $t = 2000$ for the symmetric composition, $N_A : N_B : N_{CD} = 1 : 1 : 1$. (a) Plot of RDF, $g_{AB}(r)$, against radial distance, r, for different chain lengths. Snapshots illustrating the evolution corresponding to $L_p = 8$ and 32 are provided for visual reference. (b) Scaled correlation function $C(r,t)$ as a function of r/R at $t = 2000$. (c) exhibit the time variation of length scale, $R(t)$. (d) Scaled characteristics domain sizes, R/R_0 against t/t_0. The inset shows the variation of R_s versus L_p.

In Fig. 3.8(c), the temporal evolution plot shows that the early time behavior of $R(t)$ is similar to that observed in the BCP case. For shorter $L_p = 8$, $R(t)$ shows diffusive growth ($\phi \sim 1/3$) (black curve). The black dashed line shows as a reference for the slope $\phi \sim 1/3$. For longer RCP chain lengths, the growth is slightly amplified. A transition crosses over from a diffusive growth regime to a frozen morphology. The saturation rate is notably more rapid in the presence of shorter RCP chains than their larger sizes.

The longer RCP chain length $L_p = 16$ (red curve) and $L_p = 32$ (green curve) show significant data overlap as depicted in the Fig. 3.8(d). This shows the self-similar characteristic of SF morphologies. As a result, SF segregates to a longer saturation length as the molecule size increases (while maintaining constant density). The inset shows the linear dependence behavior between R_s and L_p as theoretically predicted by the Eq. 3.5. Longer chains promote a more organized and larger clustering of SF, while shorter chains result in smaller and more dispersed SF domains.

3.4.3 Effect of composition ratio

In this section, we examine the impact of varying composition ratios of APs on the system's dynamics, specifically focusing on the SF phase separation kinetics. We report results for three different concentrations ratios: $N_A : N_B : N_{CD} = 1 : 1 : 1$, $2 : 2 : 1$, and $9 : 9 : 2$. In each case, the amphiphilic polymer chains consist of symmetric C and D compositions. The polymer chain length is fixed at $L_p = 16$, and polymeric chain rigidity is set at $k_a = 10$, $k_b = 128$. Our main focus is to understand the effect of AP components on the self-assembly of SF. This will provide essential insights into the intricate interactions between the AP composition and the resulting SF subsequent morphological formation.

The morphologies corresponding to a composition ratio of $2 : 2 : 1$ and $9 : 9 : 2$ at $t = 500$ are displayed in the two columns of Figs. 3.9(a-c) and Figs. 3.9(g-i), respectively. The analogous cross-sections are shown in the xy-plane at a fixed z in Figs. 3.9(d-f) and Figs. 3.9(j-l). For ratio $1 : 1 : 1$, time evolution snapshots are displayed in the first column of Fig. 3.2 at $t = 500$. It is evident that with a decrease in the number density of the polymeric fluid, the domain growth kinetics of SF increases substantially for all three

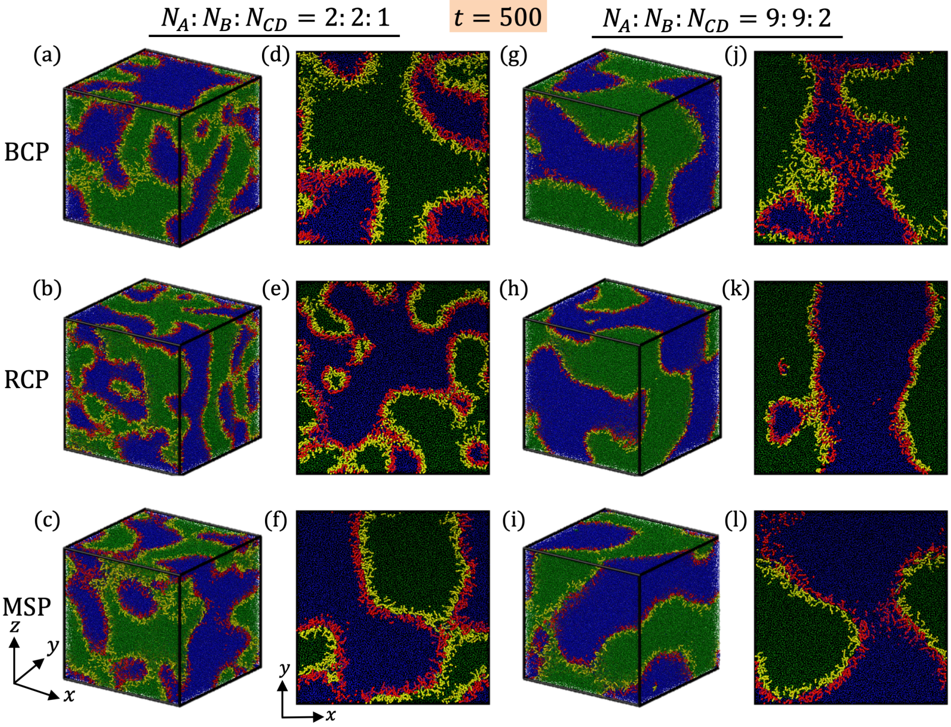

Fig. 3.9: Comparison of evolution morphologies and their $2d$ cross-section at $t = 500$ at different composition ratios, $N_A : N_B : N_{CD} = 2 : 2 : 1$ in (a-c) and (d-f), and $9 : 9 : 2$ in (g-i) and (j-l) for BCP, RCP, and MSP. The SF components, A and B are marked in blue and green in the presence of APs, with C and D components denoted in red and yellow.

AP topologies considered in our simulation. However, the cluster sizes of A-phase (blue beads) or B-phase (green beads) in the presence of RCPs appear smaller than for BCP and MSP.

To characterize the resulting SF morphologies in the presence of various topologies and compositions of APs, we plot $C(r, t)$ against $r/R(t)$ in Figs. 3.10(a-c). The scaled $C(r, t)$ plots correspond to composition ratios of $1 : 1 : 1, 2 : 2 : 2$, and $9 : 9 : 2$ are represented by the black, red, and green curves, respectively. The black curve suggests a slight deviation across all three AP topologies at lower $r/R(t)$ values. It exhibits a oscillatory pattern with an extended tail in $C(r, t)$, suggesting a higher number of interfaces exist and implying the formation of smaller domains compared to other ratios, $2 : 2 : 1$ and $9 : 9 : 2$.

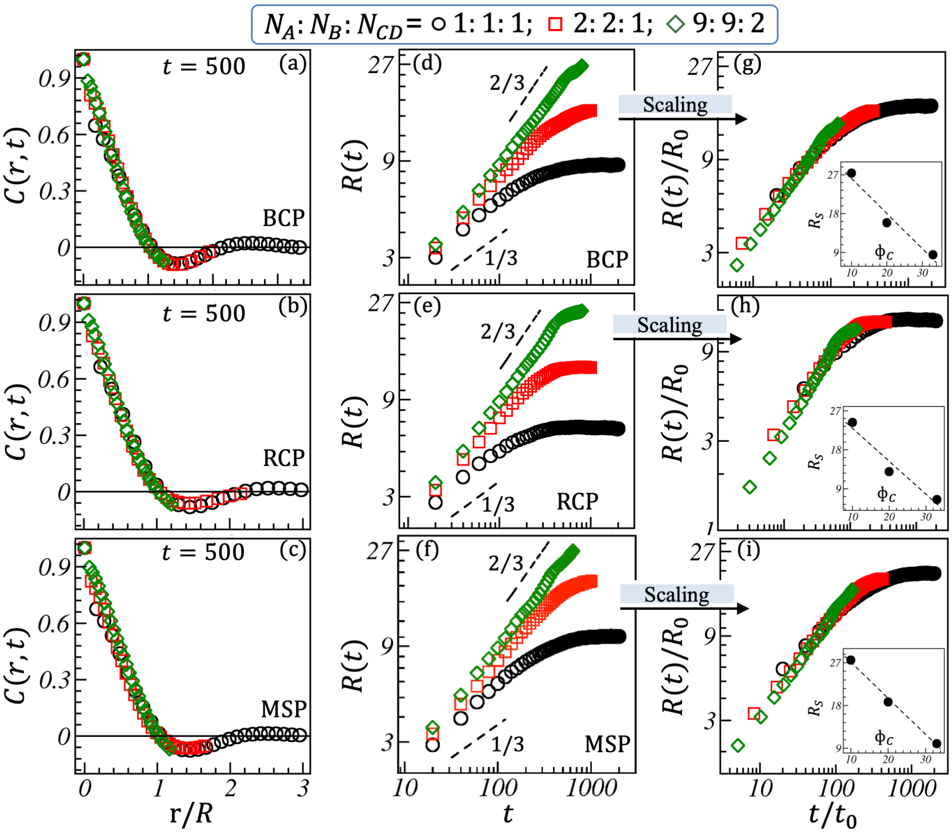

Fig. 3.10: Scaled correlation function, $C(r,t)$ vs $r/R(t)$ plots in (a)-(c), the length scale, $R(t)$ vs t plots in (d)-(f), and the corresponding scaled version of the length scale in (g)-(i) are plotted for SF morphology in the presence of BCP, RCP, and MSP. The black, red, and green symbols denoted the composition ration $1:1:1$, $2:2:1$, and $9:9:2$, respectively.

Let us compare the time dependence of the characteristic length scale, $R(t)$, for different composition ratios as shown in Figs. 3.10(d-f). Recall that for the composition ratio $1:1:1$, $R(t)$ initially follows a diffusive growth pattern ($\phi \sim 1/3$), which gradually saturates to a frozen morphology at late times. As the density of APs decreases, the interfaces become less densely covered, allowing for easier transport of SF components across the interface. This results in $R(t)$ deviating from diffusive growth, exhibiting a higher growth rate during the early times. The length scale appears to approach the regime of inertial hydrodynamic growth ($\phi \sim 2/3$) at later times without adequately transitioning into the viscous hydrodynamic regime ($\phi \sim 1$) at intermediate time. For the $2:2:1$ ratio (red curve), $R(t)$ tends to saturate at a much higher average length scale compared to the $1:1:1$ ratio. In the case of the $9:9:2$ composition ratio (green curves), $R(t)$ transitions to a frozen morphology only in the presence of RCP. However, for BCP and MSP, $R(t)$ shows a slight slowdown at later times within the simulation timeframe.

Finally, we compare the scaled characteristic length scale, $R(t)/R_0$ vs t/t_0 in Figs. 3.10(g-i). The excellent data overlap for the composition ratios $1:1:1$ and $2:2:1$, suggesting self-similar SF morphologies. However, a deviation in the green curve is observed for the composition ratio $9:9:2$, indicating minimal freezing on the length scale. The saturation length for each topology exhibits a inversely decay pattern with the composition of APs shown as $R_s \sim \frac{1}{\phi_c}$, where ϕ_c is the percentage of AP components in the system. The insets in Figs. 3.10(g)-3.10(i) clearly illustrate our Eq. 3.6 prediction.

3.5 Summary and conclusions

We have demonstrated comprehensive DPD simulation results on phase separation kinetics of binary SF in the presence of AP of three different topologies in the $d = 3$ system. Here, we investigated the effect of AP topology on the domain growth of SF and their segregation kinetics across the simple fluid interface. As a result, we obtained the following significant results.

Our results show that SF cluster size is greatly affected by AP topology, length, and concentration. The presence of RCPs exhibits a more pronounced effect on slowing down SF domain growth. With a fixed chain length, RCP has a stronger impact on SF's dynamic universality due to its unique topological constraints. In contrast, BCP and MSP have a similar effect on SF growth kinetics. Changing AP chain length at a fixed composition ratio significantly affects SF morphology and growth kinetics. Shorter chains lead to more APs, which cover the SF interface better. This restricts SF component transport and slows domain growth.

We further observed that, at a fixed composition ratio, shorter chain lengths result in a higher number of APs in the system. This increases SF interface coverage more effectively than a smaller number of longer chains. Consequently, domain growth slows down due to the restricted transport of SF components across the interface. The scaled correlation functions showed consistent scaling across all studied chain lengths and topologies, except for a moderate deviation with shorter RCP chains. This led to a more diffuse arrangement of A and B clusters. Additionally, decreasing the density of APs significantly increases the size of SF domains. RCP presence results in less AB fluid clustering than BCP or MSP, regardless of composition ratios. The corresponding scaled correlation functions deviate when the composition ratios vary significantly for any given AP. However, changing the stiffness of APs while maintaining a constant composition ratio and chain length only minimally affects SF evolution kinetics.

The characteristic length scale generally exhibited a crossover from early-time diffusive growth ($\phi \sim 1/3$) to a frozen length scale at higher to moderate concentrations for shorter chain lengths across all AP topologies studied. In these cases, the length scale saturates to a much lower value in the presence of RCP, followed by BCP and MSP. The deviation from the typical length scale observed in pure binary SF phase separation is significant. The length scale deviation during early-time diffusive growth is minimal with presence of RCP. At much lower composition ratios and moderate chain lengths, the growth law transitions to the inertial hydrodynamic regime ($\phi \sim 2/3$) at later times, without adequately entering the viscous hydrodynamic regime ($\phi \sim 1$) during intermediate time-steps of the evolution.

We hope our DPD simulation results will enable additional systematic experiments exploring the role and effect of amphiphilic polymers on the separation kinetics of these physically essential systems.